Research Article

Direct Torque Control of Induction Motor Using ConvLSTM Based on Gaussian Pillbox Surface

Sudharani Potturi [ID],[1] K. Jyotheeswara Reddy [ID],[1] Ritesh Dash [ID],[1] Ramakanta Jena [ID],[2] Vivekanandan Subburaj [ID],[3] and C. Dhanamjayulu [ID][4]

[1]*School of Electrical and Electronics Engineering, REVA University, Bangalore, India*
[2]*Department of EE, Seemanta Engineering College, Odisha, India*
[3]*Department of Electrical Engineering, National Institute of Technology Silchar, Assam, India*
[4]*School of Electrical Engineering, Vellore Institute of Technology, Vellore, India*

Correspondence should be addressed to C. Dhanamjayulu; dhanamjayulu.c@vit.ac.in

This article introduces long short-term memory (LSTM)-enabled direct torque control (DTC) for induction motor under a wide range of operation. Low-power applications of industrial drives are more as compared to high-power applications. The main objective of this paper is to address high torque, poor dynamic response, and flux ripple problems observed in low-power induction motor drives. The voltage selector switching table is replaced by LSTM encoder and embedding layer with hysteresis comparator. This will ensure robust control against induction motor disturbances and at the same time will enhance the stator flux trajectory prediction for DTC. Most of the studies describe DTC at a higher speed. In this article, the DTC has been applied to lower speed IM, typically in the range of 100 RPM. Different LSTM models have also been presented in terms of response time. A detailed comparative analysis between LSTM and fuzzy and ANFIS-based DTC has been carried out using MATLAB/Simulink model. The performance has been evaluated under steady and transient conditions as well.

1. Introduction

Variable electric drive is an integral part of industry drive system. The use of electric drives makes the industrial process more robust and reliable and reduces the cost of operation [1, 2]. This is because the industrial drive requires less electronic components while providing greater flexibility, which makes the system more reliable and adaptable to the adverse situation that occurs in industrial drives [3, 4].

Over the last four decades, DC machines were used to achieve speed control in industrial drives due to the decoupled nature of torque and flux control. This can be achieved by armature control and field control, respectively. The DC machines can provide better performance in terms of starting torque and non-linear performance during heavy load conditions. However, the presence of mechanical conversion systems such as commutators and brushes has

made it difficult to control under variable speed operation conditions [5]. A squirrel cage induction motor provides the same torque speed characteristics against a DC motor with more efficiency, and this is due to absence of slip ring and brush maintenance. Therefore, squirrel cage induction motors nowadays find applications in starting, speed changing, and speed reversal [6, 7].

To achieve better speed control in industrial drive, particularly in induction motors, many controlling methods have been developed in the past few years. With the advancement of power electronic converter techniques, many multilevel converters were invented, where variation in phase, frequency, and magnitude can be achieved while giving AC input to the induction motor for achieving variable speed and torque control [8]. Control of variable speed can also be achieved by integrating power electronics with numerical electronics. Apart from the abovementioned

points, the dynamic characteristic of an induction motor plays an important role in improving the overall system performance [9, 10].

Zhang et al. proposed a new control technique based on limit cycle control of torque and flop as a function of pulse width modulation and input DC voltage [11–13]. However, the model shows some drift at the low-frequency region. Here problem formulation is based on the efficiency optimization algorithm. The drift at extremely low-frequency operation can be compensated with the machine constant [14].

A predictive control based on simulated annealing controller has been proposed by Hete et al. for direct torque control of the induction motor [15, 16]. Here synchronous speed and voltage behind transient reactance have been used to evaluate the change in flux and torque over the transient switching period. This in turn makes the flux and torque equal to their reference value. Space vector pulse width modulation has been used for deciding the switching state of inverters [17].

Depending on the quality of system controller architecture, the speed control can be either scalar control or vector control [18]. Generally, speed of the motor depends on stator frequency and that of torque depends on the stator current. Therefore, under transient disturbances, the frequency and amplitude of stator voltage and current have to be adjusted for achieving fundamental performances [19].

The vector control method was proposed by Patel et al. According to the authors, the common form of the vector control method is the field oriented control [20, 21]. The major points which establish the vector control method are effective pulse width modulation and machine current and voltage space vector. They transformed the three-phase torque-speed quantity into a DQ coordinate time variant quantity [22]. The transformation reduces the complexity and treats the three-phase induction motor as a DC motor in achieving required data speed characteristics [23].

Single current control-based direct torque predictive control has been developed by Yang and Lu [24]. The model has been developed and tested without any coordinate transformation method as required in field oriented control. However, at zero speed conditions, it requires an additional carrier signal for the torque control method. Direct torque control uses a switching table and hysteresis band controller for controlling torque and flux. This makes the direct torque control more stable and robust. It also produces more torque and flux ripples as well.

Duty ratio control has been proposed by Kushwaha and Sharma based on field programmable gate array and digital signal processing to produce less ripple in torque and flux [25]. Huang et al. proposed a microcomputer-based controller, where both torque and flux can be controlled separately using the zero and non-zero space vectors, respectively [26]. Here the authors have checked the closed-loop stability of the proposed controller by using Lyapunov stability criteria on the parameter variations. The dynamic characteristics are evaluated with respect to the proposed controller and proposed observer under external parameter variations.

Sung et al. investigated research-based optimization techniques to increase motor efficiency by simultaneously detecting rotor flux, motor speed, and time constant [27]. Compensation with rotational back EMF by using a deadbeat controller has been presented by Muduli et al. They have also proposed a unified flux algorithm which can eliminate status flux ripple and rotor torque ripple [28]. Compensation against rotor torque and flux performance has been investigated with a low-pass filter under steady-state condition by Hadla and Santos [29]. They investigated the ripple of flux and torque under constant time series with higher sampling frequency rate.

Optimized switching strategies under inverter switches have been presented by Kennel et al. [30]. According to them, the new strategy reduces the torque ripple and increases the dynamic response against the traditional direct torque control method which uses a hysteresis controller in conjunction with PID controller. Switching between direct and indirect voltage source converter using a sliding mode controller based on direct torque control architecture has been presented by the authors. The proposed algorithm has reduced the execution time, thereby achieving better torque performance under steady and dynamic load conditions. A fuzzy logic-enabled PID controller for direct torque control has been presented by Mei et al. [31]. The authors presented a new single sensor-based direct torque control method, where the model predicts ETA current and then adjusts the predicted value based on reference to the actual current signal. Multilevel switching states for direct torque control have been proposed by the authors to reduce the torque speed ripples with the help of constant switching ripples. Discrete space vector modulation has been presented by Geyer et al. which partially compensated torque and flux ripples to improve the static and dynamic characteristics of induction motor [32].

Optimum stator flux control by reducing the reactive power drawn from the main supply system using fuzzy logic control has been presented by Papafotiou et al. [33]. A two-state modulation has been introduced between active and zero states. Adaptive fuzzy logic has been applied to evaluate the optimum duty cycle with less execution time interval. Type 1 fuzzy logic and type 2 fuzzy logic with direct torque control have also been developed and applied for evaluating the efficiency and stability of direct torque control under variable loading condition [34].

In order to enhance the performance of permanent magnet synchronous hub motor (PMSHM), a new technique based on duty cycle finite control set based on model predictive current control has been proposed by Sun et al. [35]. The advantage of the proposed model is that it can improve the characteristics of voltage vector without modulated switching pattern. Here, 12 virtual voltage vectors are generated from available six voltage vectors. This process ultimately increases the voltage selection process, thereby enhancing the steady-state performance of FCS-MPCC. The proposed new control algorithm also reduces the computation burden from 18 times to 4 times. Again, for duty cycle management, they have introduced the zero vector in one control cycle. The model has been validated using both hardware and software.

A fault-tolerant operation for PMSHM based on MPCC has been proposed by Sun et al. [36]. In the proposed topology, decomposition occurs for normal vector space transformation matrix. The operation can be achieved without the knowledge of controller in vector space. The change in vector space from $\alpha - \beta$ to $x - y$ subspace has been obtained based on the phase difference between normal operating condition and open circuit phase voltage. Unlike [35], here 24 virtual vectors from 6-phase, two-level inverter have been obtained by decomposing 64 voltage vectors. This reduces the weight function required for each node to balance the vector space.

A deadbeat predictive stator flux control (DPSFC) method for an in-wheel PMSM drive is proposed [37], which can lower steady-state tracking error and improve drive's robustness. A comparative study of traditional deadbeat control and proposed deadbeat control with respect to stator flux variation, inductance, and resistance of stator is presented. Usually, deadbeat controls are best suited for nonlinear systems. When there is a parameter mismatch, the system experiences disturbances, and to calculate the same, a reduced-order observer is embraced. Also, these estimated disturbances are applied as feedforward compensations for stator voltage to reduce tracking error of actual and reference values. The conventional deadbeat current controls will not emphasize the effect of delay compensation, whereas in the proposed model, one-step delay compensation is applied to revamp the control accuracy. The current flux values are replaced by the predicted values of flux linkage in the next step. The simulation and hardware results (prototype) are presented in terms of flux linkage error rate. The results showcase that the proposed model has less error rate when compared to the traditional control. Sun et al. [38] proposed a FPS-PLL (finite position set-phase locked loop)-based MPCC (model predictive current control) scheme to control permanent magnet synchronous hub motor (PMSHM). In this method, addition of FPS-PLL makes the control sensor control less. The appreciable feature of MPCC is that we can directly measure the control variable, current, whereas in DTC, we need to calculate the stator flux and torque from the measured values of stator voltage and currents. Also, in the speed loop, PI controllers are replaced by sliding mode controller which has the virtue of suppressing disturbances in the speed. The MPCC constitutes (i) EMF equation formation: in which an equation is formed to calculate back EMF with inherited quality of improved tolerance range of 50%; (ii) delay compensation: to compensate the delay and increase the accuracy, the Kriging model is used; and (iii) optimal vector selection and vector duration: the optimal non-zero vector can be obtained by calculating the reference voltage (using deadbeat principle) and its positioning sector. In the next step, the optimum vector duration is calculated by deriving cost function and making it equal to 0 so that results are obtained with least possible errors. To make the system more robust and to be independent of machine parameter changes, FPS-based PLL algorithm is incorporated in the proposed model. A comparative study of experimental results for conventional and proposed MPCC is presented by the authors which shows that the proposed

model offers less torque ripples and speed distortions and lower current THD. These results are achieved by the authors without compromising the dynamic performance of the drive. The advantages of this work includes reduced in weight coefficient evaluation time and inductor fault tolerance.

The literature review presented over here reveals that a number of research studies have been carried out globally to reduce total harmonic distortion and improve the quality of drive output. In this research work, three machine learning algorithms have been compared to find the best performance of the controller. Adaptive neuro fuzzy inference system, neural network, and long short-term memory along with PID controller and hysteresis band have been used to find the performance of the proposed controller in reducing ripple of flux and torque. The contribution made in the research article can be categorized into the following points.

(i) LSTM-DTC trajectory is modeled for best tuning of the parameter.

(ii) Hysteresis comparator is modeled to effectively compute the 8-state variables.

(iii) 3×9 encoder has been modeled to evaluate the boundary condition leading to trajectory evaluation for LSTM-DTC.

2. Problem Formulation

The use of hysteresis controller in the frequency sampling techniques produces pseudo-random overshoot, hence making the system response sluggish. Thus, the operation can be made efficient by making the system dynamic instead of stationary. Time series prediction can be used in predicting the future values based on their data distribution, mean variance, and skewness.

Again from the stationary reference frame, the stator and rotor flux can be written as

$$\begin{cases} \widehat{\Psi}_{sa} = \int \left(V_{s\alpha} - R_{s\alpha} i_{s\alpha} \right) \mathrm{d}t, \\ \widehat{\Psi}_{sb} = \int \left(V_{s\beta} - R_{s\beta} i_{s\beta} \right) \mathrm{d}t, \end{cases} \tag{1}$$

where ψ_{sa} represents stator flux in α–reference frame and ψ_{sb} represents stator flux in β–reference frame. $V_{s\alpha}$ and $V_{s\beta}$ represent the stator voltage in α, β coordinate. $i_{s\alpha}$ and $i_{s\beta}$ represent the stator current in $\alpha\beta$ coordinate. $R_{s\alpha}$ and $R_{s\beta}$ represent the resistance in α, β coordinate.

$$\begin{cases} \widehat{\Psi}_{ra} = \left(V_{r\alpha} - R_{r\alpha} i_{r\alpha} \right) \mathrm{d}t \\ \widehat{\Psi}_{rb} = \left(V_{r\beta} - R_{r\beta} i_{r\beta} \right) \mathrm{d}t, \end{cases} \tag{2}$$

where ψ_{ra} and ψ_{rb} represent rotor reference flux in $R_{s\alpha}$ and $R_{s\beta}$ coordinates and $V_{s\alpha}$ and $V_{s\beta}$ represent the rotor voltage in α, β coordinate. Similarly, $i_{r\alpha}$ and $i_{r\beta}$ represent the rotor current in $\alpha\beta$ coordinate. $R_{r\alpha}$ and $R_{r\beta}$ represent the resistance in α, β coordinate.

Considering (1) and (2), the torque equation can be written as

$$T = P\left(\widehat{\Psi}_{s\alpha} i_{s\beta} - \widehat{\Psi}_{s\beta} i_{s\alpha}\right). \tag{3}$$

Equations (1) and (2) can be used as a statistical model for short time forecasting. However, due to multivariate regression analysis, evaluating the control flux becomes a tedious task. Therefore, the computational intelligence-based approach can be used to find the best solution. The main objective is to find optimization coefficient for the mathematical function. Some of the assumptions required for parametric analysis are

  (i) Drift parameter.
  (ii) Vertical curve.
  (iii) Bounded hysteresis time series interval.

Mathematically, the estimated torque can be written as

$$T_p(t) = T_p(t) + T_0(t) + T_s(t), \tag{4}$$

where $T_p(t)$ represents the available present torque at the machine shaft at time t_{n-1} as measured by tachogenerator. $T_0(t)$ represents the influenced torque as developed from variation in stator flux and $T_s(t)$ is the complex variable adopted by rotor due to interaction of stator and rotor flux. Here α, β equivalent of rotating DC components have been used as the temporal influential agents in profile modeling. The stochastic time variant differential equation for equation (4) can be represented as

$$dT_t = \mu\left(T_t, t\right)dt + \sigma\left(T_t, t_0\right)dW_t + dq\left(T_t, t\right), \tag{5}$$

where T_t represents the instantaneous torque in the torque series data defined over a time interval of dt. dT_t represents the Wiener process. So, according to the Wiener process, the instantaneous torque can either be changed to 0 or 1 depending on the random walk in discrete time interval. The objective here is to make the system continuous everywhere but not differentiable anywhere. This results in a zero mean distribution and unit variance which results in a Gaussian surface. In order to achieve this condition, a non-linear system with drift parameter as shown in equation (6) has been considered.

$$\mu_p\left(T_t, t\right) = (\alpha - \beta T_t). \tag{6}$$

Among different types of available transformation methods, for transferring non-normal variables into normal variable, the Box–Cox [39, 40] transformation can be used. Therefore,

$$f(p_t) = \begin{cases} \alpha_1 + \beta_1 dT_t \text{ for } dT_t \leq z - s, \\ \alpha + \beta b dT_t + c dT_t^2 \text{ for } dT_t \leq (z - s, z + s), \\ \alpha_2 + \beta_2 dT_t \text{ for } dT_t \geq z + s, \end{cases} \tag{7}$$

where α_1, α_2 and β_1, β_2 represent the intercepts and slope, respectively. Similarly, the leading demand slope becomes

$$dT_t = (\alpha - \beta T_t)dt + \sigma \, dw_t, \tag{8}$$

where β represents the mean reversion. Therefore, equation (5) can be written as d/dt instead of dt variables.

$$\frac{dT_t}{dt} = \mu_p\left(T_t, t\right)dt + \sigma\left(T_t, t\right)dw_t, \tag{9}$$

and that of initial reversible torque:

$$T_t(0) = T_0. \tag{10}$$

For validating the effectiveness of continuous time series data of a non-differentiable quantity, the following conditions must be satisfied.

  (i) Condition 1: boundary condition must be valid under time series interval.
  (ii) Condition 2: $[0, T]$ interval needs to be effectively considered.
  (iii) Condition 3: the equation needs to be partitionable at each point.

The perfect stochastic differential equation using equations (9) and (10) can be written as

$$T_t = T_0 + \int_0^t \beta T(s)ds + \int_0^t \alpha T(s)dw + \int_0^t \sigma T(s)dq. \tag{11}$$

By considering condition 2, the expanded time series data become

$$[0, T] \epsilon t = 0 \longrightarrow \infty, \tag{12}$$

$$Tp(t) = 0 = t_0 < t_1 \cdots < T_{\max} = T. \tag{13}$$

On fixing the value of μ_p in equation (9) to $\mu_p \epsilon [0, 1]$, the partition set of equation becomes

$$\mu_K = (1 - \mu)t_K + \mu \epsilon_{K+1} \ldots \ldots \ldots (K = 0, 1, 2, \ldots \ldots \ldots m - 1). \tag{14}$$

Therefore, the differentiable partition equation becomes

$$R = R(T(p), \mu) = \sum_{K=0}^{m-1} w(\mu_k)\left(w(\mu_{K+1}) - w_k(N_K)\right). \tag{15}$$

Derived equation (15) is a close approximation variable of Riemann sum approximation. It calculates the area under the curve, and in this paper it is hysteresis band. The sub-interval approximation can be increased by decreasing the width of "Δ" value as per the following equation:

$$\Delta T = \frac{T_n - T_{n-1}}{n}. \tag{16}$$

Equation (15) can be realized in terms of pollination algorithm; accordingly, let us consider two sets of flower interval of $[x_0, y_0]$, which is again in the range of $[0, \infty)$. Here "0" represents the bounded and "∞" is the unbounded region. Hence, the specific set of equation becomes

$$TP(t)^n = [x_0 = t_0^n < t_1^n \cdots < t_{\max}^n = T_0]. \tag{17}$$

Equation (17) becomes valid when $|TP(t)^n| \longrightarrow 0$ and $n \longrightarrow \infty$. Therefore, equation (17) can be simplified into

$$Q = \mu_P(T_t, t) = \sum_{K=0}^{m_n-1} \left[(w(t_{K+1}^n)) - w(t_K^n) \right]^2. \quad (18)$$

Again simplifying equation (15) by varying "Q" in equation (18), it becomes

$$E\left[(Q_n - (y_0 - x_0)^2) \right] = \sum_{K=0}^{m_n-1} \sum_{j=0}^{m_n-1} E\left[w(t_{K=1}^n) - w(t_K^n)^2 - (t_{K+1}^n - T_K) \right] \left[\left(w(t_{j+1}^n) - w(t_j^n)^2 \right) - \left(t_{j+1}^n - t_j^n \right) \right]. \quad (20)$$

On cancelling the non-linearity variable and finding mathematical solution to equation (20), it can be further reduced into

$$E\left(Q_n - (x_0 - y_0)^2 \right) \le C_K \sum_{K=0}^{m_n-1} \left(t_{K+1}^n - t_K^n \right)^2, \quad (21)$$

$$Q_n - (y_0 - x_0) = \sum_{K=0}^{m_n-1} \left[(w(t_{K+1}^n)) - w(t_K^n) \right]^2 - (t_{K+1}^n - t - K). \quad (19)$$

Now the energy content of equation (19) becomes

or

$$E\left(Q_n - (x_0 - y_0)^2 \right) \le C_K \left| T_P^n(t,h) \right| (y_0 - x_0) \longrightarrow 0. \quad (22)$$

The derived optimization equation becomes

$$E\left(Q_n - (x_0 - y_0)^2 \right) = \sum_{K=0}^{m_n-1} w(\mu_K^n)\left(w(\mu_K^{n+1} - \mu_K^{m+1}) \right), s.t = \begin{cases} \lim_{n \to \infty} E\left(Q_n - (x_0 - y_0)^2 \right) \\ = \dfrac{w(T)^2}{2} + \left(\mu - \dfrac{1}{2} \right) T; \\ t_K^n \le z_K^n \le t_{n+1}^n. \end{cases} \quad (23)$$

3. Benchmarking Model

3.1. Fuzzy + PID Controller. Hysteresis band-based PID controller generates high torque and ripple in the flux. This is because of the continuous operation of switching vector over the sample for entire period of operation. Fuzzy logic-based switching pattern generation will provide smooth switching sequence with less ripple in flux and torque. As discussed in the preceding section, the non-linear behaviour of switching pattern is a function of two errors such as flux error and torque error along with stator flux angle. Therefore, rule-based fuzzy logic supported by PID controller can be designed. Figure 1 shows the basic building diagram of fuzzy-enabled DTC.

Here torque error has been evaluated using PID controller supplied from speed error as a crisp variable to fuzzy logic controller. Similarly, another stator flux error and another stator flux angle will serve as crisp variables 2 and 3, respectively. The fuzzy rule-based controller will work on these crisp variables only after fuzzification using seven membership functions.

Here seven membership functions from negative large (NL) to positive large (PL) have been used. Here two types of waveform such as trapezoidal type for NL and PL algorithm triangular type waveform for all other membership functions have been used. Six sectored stator flux trajectories from Q_1 –Q_6 comprising each 30^0 in each half have been used.

A threshold error torque level of 5 N-m has been used so that the crisp variable PL becomes "1" and it will change to next transition state of "0" as soon as the threshold level decreases to 0. Trivectored error of mean deviation of 0.02 has been used from NS to PS. So, when torque error falls under 0.02, the PS will be set to 1 and NS will be set to 0. The stator flux error has been assigned to three variables such as 1, 0, and −1. Therefore, the variable for crossover area was determined using min-max concept. Figure 2 shows the voltage distribution pattern with respect to Membership function (MF).

A total of 147 rules have been framed to establish the AND and OR segmentation. The operating section will be evaluated after cross overlapping of stator flux error and torque error.

Figure 3 shows the torque produced by motor under two different conditions such as normal and abnormal conditions. As observed, with increase in speed, the torque is reduced to 1.2 N-m. A zoomed version of the torque curve is also shown in Figure 3. At about 0.295 seconds, a sudden change in the curve has been observed, and this is due to change in the membership function in the Sugeno fuzzy controller. Similarly, at about 0.5 seconds, again torque increases due to decrease in motor speed because of voltage change. At about 0.795 seconds, for sample-9, the state variables are the same and hence no changes in the torque state are observed.
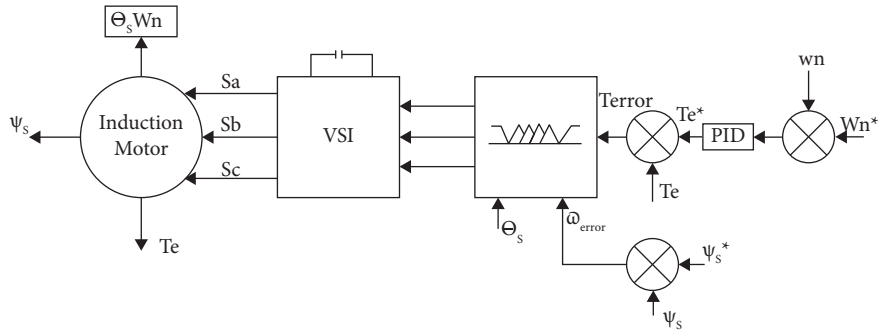
Figure 1: Detailed block diagram of fuzzy-PID DTC of IM.
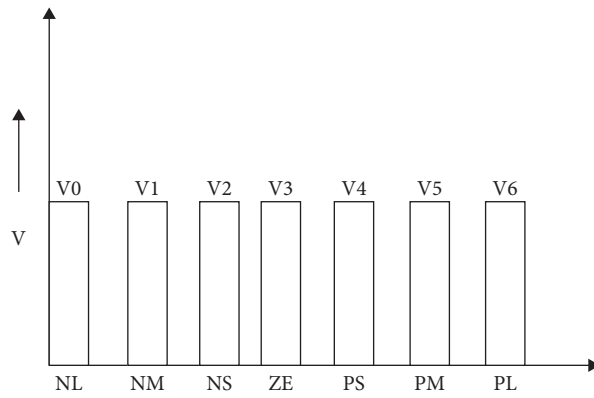

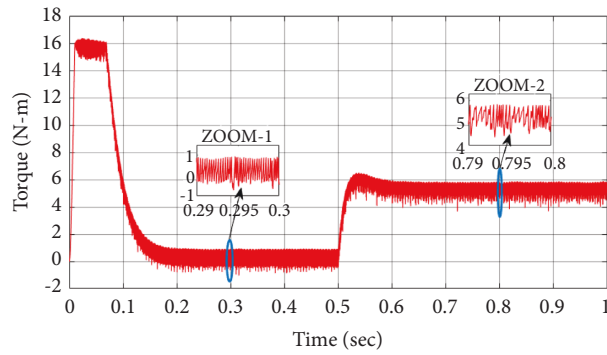Figure 2: Voltage distribution pattern.

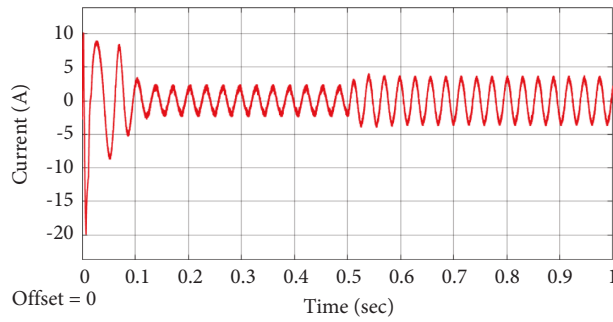Figure 3: Torque produced by motor under fuzzy-DTC.

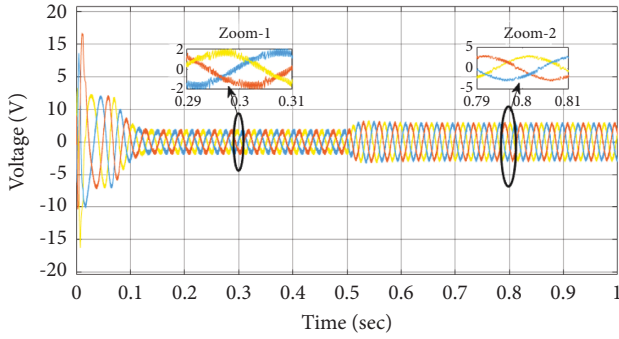Figure 4: Current waveform at input terminal of motor under fuzzy-DTC.

FIGURE 5: Voltage waveform at input terminal of motor under fuzzy-DTC.

Figures 4 and 5 show the current and voltage curve of fuzzy-enabled DTC at motor input terminal. As mentioned earlier, a state change transition occurs at 0.5 seconds; therefore, an increase in current has been noticed. Here only one phase is shown for simplicity and analysis point of view. Similarly, in voltage wave, the changes have been observed. Another observation regarding the voltage waveform is that a lot of noise is present. The voltage harmonic analysis presented in Figure 6 shows that the total harmonic distortion is about 14.32% which is little higher.

Stator flux trajectory is shown in Figure 7. It is observed that a slope deviation of 0.377 occurs in each transition. Again, the statistical analysis for flux trajectory under fuzzy-DTC controller is shown in Table 1. A RMSE of 0.24 has been observed for cluster-3, and state change occurs for sample-2 and sample-4. Similarly R^2 – error for one sample was found to be 1.0. This enables the authors to think for ANFIS-DTC. In the next section, ANFIS-DTC has been presented as 2nd benchmarking model.

3.2. ANFIS. Generally, an induction motor poses two control techniques for direct torque control. In torque control mode, reference torque and actual torque act as an input to ANFIS, whereas in speed control mode, actual speed and reference speed would act as an input to the ANFIS control. Speed control mode requires a PI controller for amplification shoot overshoot improvement.

ANFIS is a hybrid controller having property of both neural network and fuzzy logic. The membership functions were decided by the neural network if and only if the mapping from input to output is available. To create a fuzzy inference system, a five-layer structure has to be modeled comprising fuzzy layer, product layer, normalized layer, defuzzification layer, and final output layer. The detail process diagram is shown below.

Figure 8 shows a five-layer model of ANFIS. Here, two intermediate circular nodes represent dynamic node and square node represents fixed node.

The output of the first layer as a function of x and y can be represented as

$$O_{1,i} = \mu_x(X) \text{ for } i = 1, 2, \ldots n$$
$$O_{1,i} = \mu_x(Y) \text{ for } i = 1, 2, \ldots n. \tag{24}$$

The second layer in ANFIS represents about fuzzy rule written in if-then rules. Most of the rules are of Sugeno type of first order. The first two rules based on if-then are

Rule 1: if x is A_1 and y is B_1, then $f_1 = P_1 x + q_1 y + r_1$.
Rule 2: if x is A_2 and y is B_2, then $f_2 = P_2 x + q_2 y + r_2$.

In rule 1 and rule 2, x and y denote the input to the ANFIS representing reference torque and actual torque. A and B are the rule-based fuzzy sets and f_1, f_2 represent the first-order polynomial. Applying fuzzy set error multiplication to the existing variables, the output of layer-2 becomes

$$O_{2,i} = \mu_A(x)\mu_B(x), \quad i = 1, 2, 3, 4. \tag{25}$$

The output of layer-2 is normalized by the weight function of layer-3. Therefore, the normalized output becomes

$$0_{3,i} = \frac{w_i}{\sum_{i=1}^{n} w_i}, \quad i = 1, 2, 3, 4. \tag{26}$$

The normalized weight output in equation (27) will be evaluated against each fuzzy rule under interference of external parameters. Therefore, equation (27) can be further modified.

$$O_{4,i} = \overline{w}(p_1 x_1 + p_2 x_2 + \cdots p_4 x_4 + q_1 y_1 + q_2 y_2$$
$$+ \cdots q_4 y_4 + r_i), \quad i = 1, 2, 3, 4. \tag{27}$$

Like equation (28), four sets of equations will be summed up and their average weighted sum will be evaluated as a numerical variable equal to non-fuzzy part. Therefore, output of layer-5 becomes

$$O_5 = \sum_{i=1}^{n} \overline{w} f_i. \tag{28}$$

In order to execute the ANFIS-based DTC, an experimental investigation has been carried out with DTC-based PI controller. The output of DTC system has been divided into 70% for training dataset and 30% for testing data. Membership functions were adjusted through forward and backward speed. During fuzzy inference, if any redundancy was noticed, it was adjusted through backpropagation algorithm.

Figure 9 shows the torque produced by motor under ANFIS-DTC. As observed, with increase in speed, the torque is reduced to 1.2 N-m. A zoomed version of the torque curve is also shown in Figure 9. At about 0.295 seconds, a sudden change in the curve has been observed, and this is due to change in the membership function in the Sugeno fuzzy controller. Similarly, at about 0.5 seconds, again torque increases due to decrease in motor speed because of voltage change. At about 0.795 seconds, for sample-9, the state variables are the same and hence no changes in the torque state are observed.

Figures 10 and 11 show the current and voltage curve of ANFIS-enabled DTC at motor input terminal. As mentioned earlier, a state change transition occurs at 0.5 seconds; therefore, an increase in current has been noticed. Here only
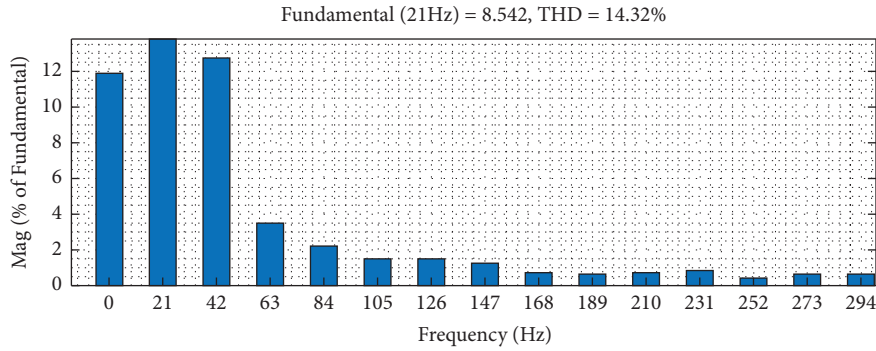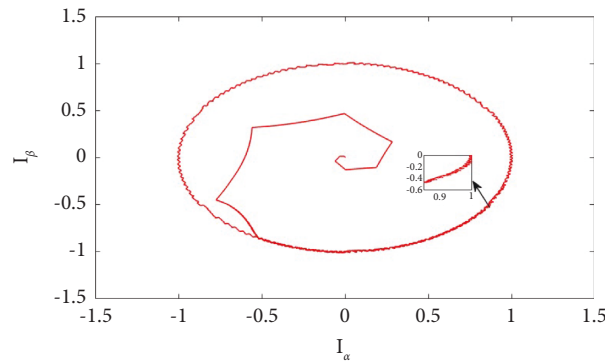
FIGURE 6: THD of voltage under fuzzy-DTC.

FIGURE 7: Stator flux trajectory under fuzzy-DTC.

TABLE 1: Statistical analysis of stator flux trajectory for fuzzy-DTC.

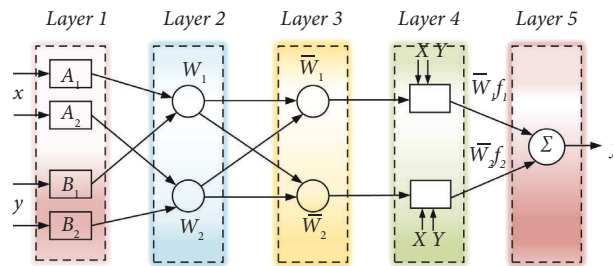| Cluster	RMSE	R2-error	MSE	MAE	Remarks
C-1	0.23	0.98	0.07	0.82	s-1
C-2	0.24	0.99	0.04	0.81	s-2
C-3	0.24	0.97	0.06	0.81	s-2
C-4	0.24	1.00	0.07	0.82	s-4
C-5	0.26	0.99	0.07	0.83	s-5

FIGURE 8: Layer model of ANFIS.

one phase is shown for simplicity and analysis point of view. Similarly, in voltage wave, the changes have been observed. Another observation regarding the voltage waveform is that a lot of noise is present. The voltage harmonic analysis presented in Figure 12 shows that the total harmonic distortion is about 11.73% which is little higher.

Stator flux trajectory is shown in Figure 13. It is observed that a slope deviation of 0.29 occurs in each transition.

Again, the statistical analysis for flux trajectory under ANFIS-DTC controller is shown in Table 2. A RMSE of 0.21 has been observed for cluster-3, and state change occurs for sample-2 to sample-5. Similarly R^2 – error for almost all samples was found to be 0.99 except for some samples at clusters C-1 and C-4. This enables the authors to think for LSTM-DTC. In the next section, LSTM-DTC has been presented.
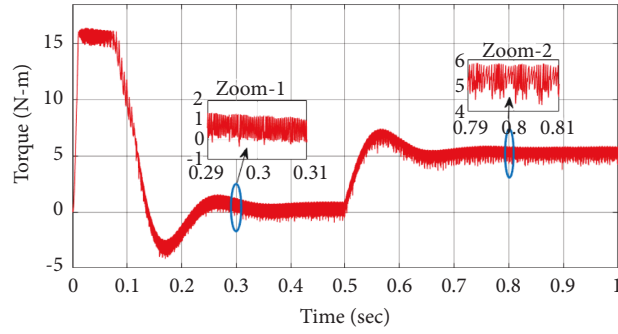
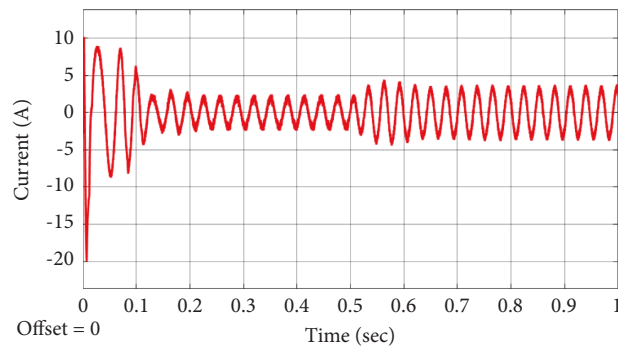FIGURE 9: Torque produced by motor under ANFIS-DTC.

FIGURE 10: Current waveform at input terminal of motor under ANFIS-DTC.
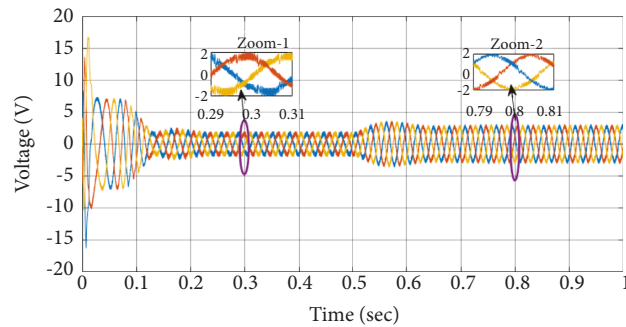

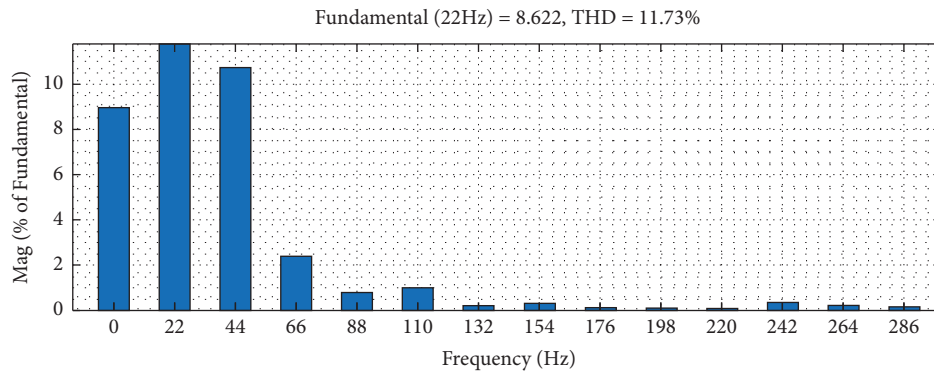FIGURE 11: Voltage at waveform at input terminal of motor under ANFIS-DTC.

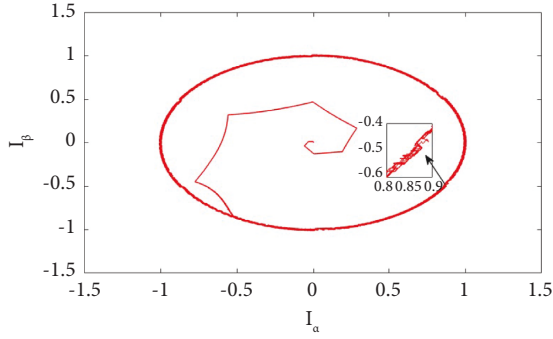FIGURE 12: THD of voltage under ANFIS-DTC.

Figure 13: Stator flux trajectory under ANFIS-DTC.

Table 2: Statistical analysis of stator flux trajectory for ANFIS-DTC.

Cluster	RMSE	R2-error	MSE	MAE	Remarks
C-1	0.19	0.98	0.032	0.41	s-3
C-2	0.21	0.99	0.041	0.57	s-4
C-3	0.21	0.99	0.044	0.56	s-4
C-4	0.21	0.98	0.042	0.56	s-4
C-5	0.22	0.99	0.042	0.56	s-1

4. Result Analysis

One of the easiest methods for the DTC is using hysteresis controller. However, the fluctuation in the steady state static output is a problem. This can be avoided by adding additional damping circuitry in conjunction with main hysteresis controller. In order to achieve proper control, it requires stator flux and torque for hysteresis controller along with rotor speed. The typical sampling rate for hysteresis band controller is 40 kHz which is 4 times higher than PWM sampling rate. Table 3 represents the motor parameters used for simulation analysis.

It can be understood that the fluctuation in the controller signal can be limited if control action can be made dependent on input data, past error, and output of controller. All these features can be integrated to a sequence learning process. LSTM is a type of sequence learning that falls under the category of recurrent neutral network (RNN). Because of its memory about the past data, it processes the trajectory data and prepares the new predictive trajectory. Hence, trajectory refers to the stationary flux distribution. Because of the gradient vanishing property of RNN, it is not popular in capturing long-term memory. However, LSTM retains the error values in its memory and continues the gradient flow.

Figure 14 shows the schematic structure for the flux analysis using LSTM-DTC. As compared to RNN-DTC, in LSTM-DTC, three extra features have been added such as forget gate, input gate, and output gate. Two activation functions are shown in Figures 14 and 15. The actual stationary flux and reference stationary flux will act as input to the forget gate. If the actual flow deviation $\Delta\Psi$ is greater than 5.2, then that particular instant flux will not be considered as an input to LSTM gate. This is to only keep memory active around the trajectory. This can be achieved either by multiplying the actual flux with 1 or 0. 1 is used if it is required to

Table 3: Motor parameters for simulation analysis.

Sr. no.	Parameter	Symbol	Rating	Unit
1	Nominal power	Pn	3.2	kwatt
2	Nominal voltage	V	400	Volt
3	Nominal current	I	6.74	Amp.
4	Rated frequency	F	50	Hz.
5	Stator flux (linkage flux)	Phi	0.66	Wb
6	Rotor DC resistance	Rr	1.77	ohm
7	Stator DC resistance	Rs	1.24	ohm
8	Mutual inductance	Lm	0.19	mH
9	Rotor inductance	Lr	0.091	mH
10	Stator inductance	Ls	0.091	mH
11	Rated normal speed	N	1500	rpm
12	Pole pairs	p	2	Nos.

maintain the data in memory or else 0. Based on the above discussion, the LSTM network architecture becomes the following. Activation gate input:

$$i^t = g\left(w_i^t + p_i y^t q_i c^{t-1} + b_i\right). \tag{29}$$

Output gate:

$$l^t = \sigma\left(w_e^t + p_l y^t q_e c^{t-1} + b_l\right). \tag{30}$$

Forget gate:

$$f^t = \sigma\left(w_f^t + p_f y^t c^{t-1} + b_f\right). \tag{31}$$

Torque error and stator flux error evaluation and six-sector evaluation of linguistic variable are shown in Algorithms 1 and 2. Three gate functions in terms of variable and bias from equations (31)–(33) are shown in process flowchart in Figure 16. Likewise, the neutral weight becomes the following (combining all gate weights). Input weight:

$$w_i, w_e, w_f \varepsilon R^{NXD}. \tag{32}$$

Output weight:

$$p_i, p_l, p_f \varepsilon R^{NXD}. \tag{33}$$

Memory weight:

$$q_i, q_l, q_f \varepsilon R^{NXD}. \tag{34}$$

Bias weight:

$$b_i, b_l, b_f \varepsilon R^{NXD}. \tag{35}$$

Now based on equations (34)–(37), the new memory function becomes

$$c^t = i^t l^t + c^{t-1} f^t, \tag{36}$$

$$\ddot{D}_{b1} = D_{b1} f c^t. \tag{37}$$

In general, the output flux control signal becomes

$$y_0 = f\left(\sum_{i=1e=1}^{N} R_i^N R_{e+1}^N + \sum_{F=1}^{j} MF^{147}\right). \tag{38}$$
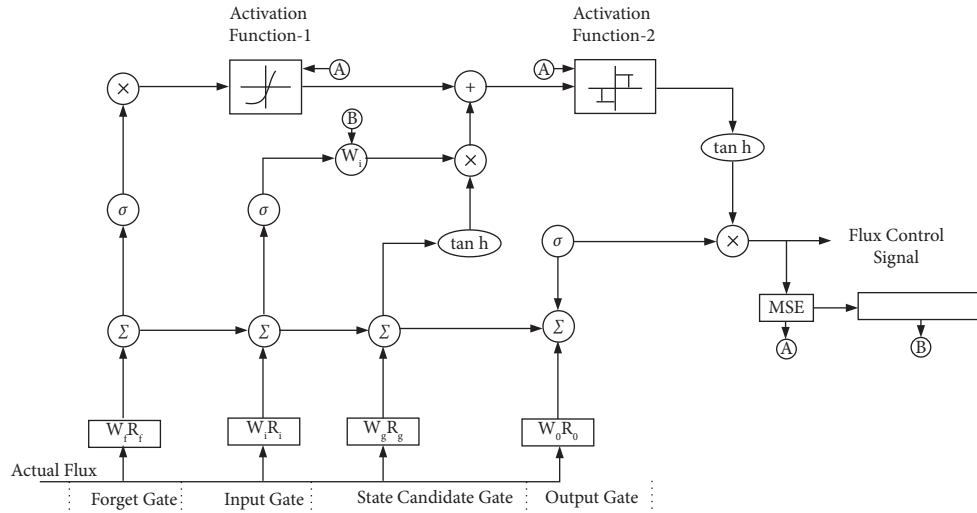
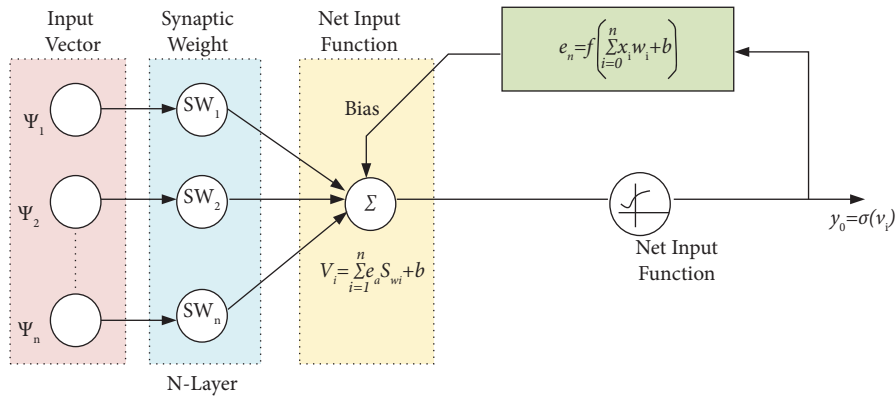Figure 14: Schematic structure for flux analysis using LSTM-DTC.

Figure 15: Schematic structure for activation function.

Equation (38) is the output flux control signal, where the output depends on both present input and past memory saved error signal. As the LSTM consists of four memory nodes, the error encountered in the LSTM nodal evaluation must be propagated to all the nodes. Hence, the backpropagation model for transferring the error to all the nodes has been applied. As trajectory track is the objective of this research work, time deviation of backpropagation algorithm has been implemented. The schematic diagram of the detailed model putting LSTM into loop is shown in Figure 17.

Two rounds of evaluation have been carried out for station flux trajectory and rotor flux trajectory analysis. Station flux trajectory evaluation with mu of 0.2 and 0.27 has been conducted. 12-point evaluation of each 30° has been examined. Each point denotes one sample space. Table 4 represents window-1 for stator flux predictions using LSTM with mu-0.22. Hence, it is observed that for sample $\delta(P - \delta)$ of 240 °, the root mean square is the smallest one of 0.347, and relative error becomes 13.37%. Similarly, highest RMSE becomes 2.254 and that of relative error becomes 17.3%. The lowest relative error has been observed for sample-6 of 11.91 at an angle of 180°.

Table 5 shows the second window of stator flux prediction (LSTM with mu = 0.27). Here sample-7 has RMSE of 1.29 and relative error of 15.39. In Table 5, the smallest relative error was found to be 12.64 for sample-9 with an angle of 270°. This shows that sample-8 and sample-7 from Tables 4 and 5 exhibit highest transition in terms of switching frequency. However, the switching frequency is relatively small as compared to hysteresis controller and benchmarking model.

Table 6 shows the rotor flux prediction, LSTM with $N = 0.9$. Here, the RMSE between the actual flux density and that of 1.811 for sample-3 is given. In most of the samples, the actual and predicted flux densities are close to each other. This happens because of the forget gate used in LSTM network. The response time becomes sluggish towards the end of sample-12. This is because of the backpropagation algorithm and sharing of output layer error among each node. All the intermediate node weight functions are deleted for creating memory space for integral multiple of 30° sample.

Table 7 shows the rotor flux density, LSTM with mu = 0.12. The relative error is 12.03% for sample-4. Similarly, maximum RMSE has been noticed at 1.631.
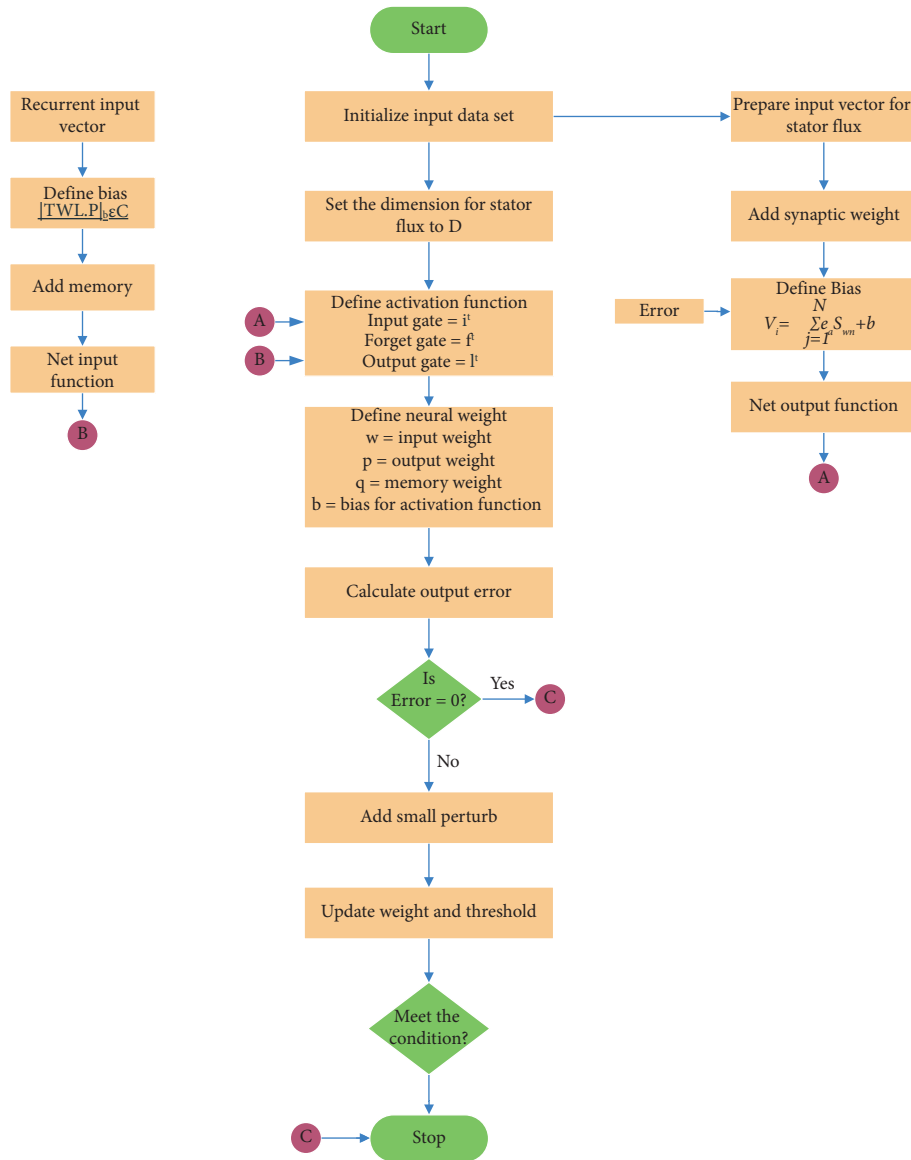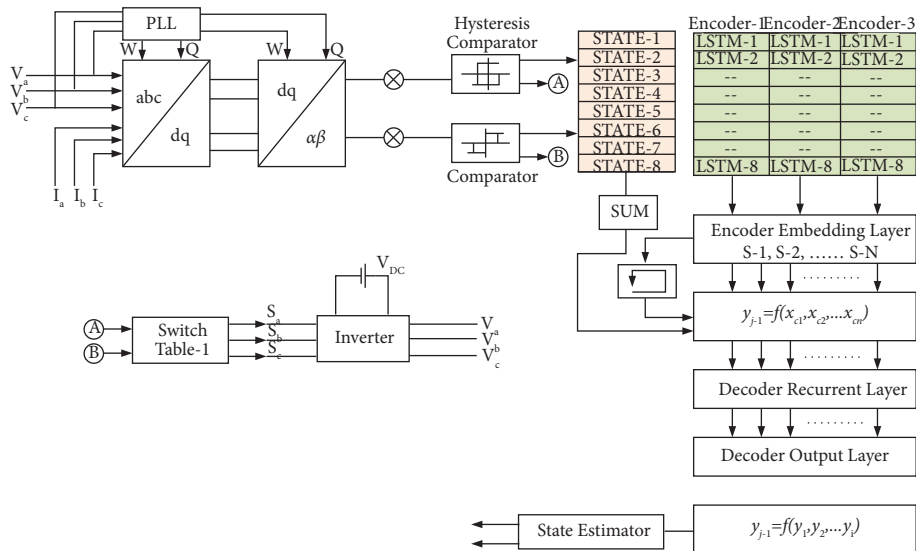
FIGURE 16: Flowchart of LSTM procedure.

FIGURE 17: Schematic diagram of LSTM-enabled DTC for 8-state variable.

Require: T_er, W_er, θ_s
Ensure: 3 Variable state transition pattern
    for PL = 1 **do**
      for NL = −1 **do**
        for Wer = 0 **do**
          Evaluate $T_e r$ and θ_s
        end for
      end for
    end for
    Weight $w_i = \min(\delta T\_er, \delta W\_er, \theta\_s)$
    $\theta\_x V\_x = \max(\theta\_x - 1 V_{x-1}, \theta_x V_x)$
    for PL = −1 **do**
      for NL = 1 **do**
        for Wer = 0 **do**
          Evaluate the membership function, $M_f^{147}(\theta_x V_x) = M\_L$
        end for
      end for
    end for
    if $(M_{L-1}^{t_0} - M_L^{t_1}) \le 0.02$ **then** break
    else $(M_{L-1}^{t_0} - M_L^{t_1}) \le 0.02$
    end if

ALGORITHM 1: Torque error and stator flux error evaluation.

Require: Linguistic Variable, MF
Ensure: Sector Selection
    $x \leftarrow IFD(M_F^{147})$
    $MF_2 \leftarrow \max(X_1, X_2, \ldots X_M)$
    $MF_2 \leftarrow \max(X_1^{t-1}, X_2^{t-1}, \ldots X_M^{t-1})$
    $P \leftarrow$ Calculate Cluster Member
      DO Until MF from ZE is Found
      if $e_{\text{error}} \le 0.01$ **then**
        V_0 is output
      else
        Delete the result and RESET
      end if

ALGORITHM 2: Six-sector evaluation for linguistic variable.

TABLE 4: Window-1: stator flux prediction (LSTM with mu = 0.22).

Cluster	Response time (s)	Rho	Flux density		Error	
			Actual	Pden	RMSE	RF%
P-1	0.029	0.58	0.46	0.47	2.331	17
P-2	0.033	0.61	0.47	0.47	2.311	15.2
P-3	0.047	0.68	0.44	0.46	2.254	17.3
P-4	0.051	0.72	0.43	0.45	2.237	17.1
P-5	0.054	0.75	0.39	0.39	1.861	14.03
P-6	0.059	0.78	0.36	0.39	1.453	11.91
P-7	0.064	0.79	0.31	0.34	1.329	21.15
P-8	0.068	0.80	0.28	0.28	0.347	13.37
P-9	0.069	0.81	0.22	0.23	1.167	15.02
P-10	0.072	0.83	0.16	0.14	1.363	13.86
P-11	0.077	0.86	0.17	0.16	1.268	16.33
P-12	0.078	0.86	0.17	0.16	1.269	16.37

TABLE 5: Window-2: stator flux prediction (LSTM with mu = 0.27).

Cluster	Response time (s)	Rho	Flux density		Error	
			Actual	Pden	RMSE	RF%
P-1	0.030	0.59	0.31	0.32	1.8	16.68
P-2	0.034	0.73	0.32	0.32	1.78	15.76
P-3	0.046	0.74	0.37	0.38	1.80	15.58
P-4	0.053	0.75	0.34	0.36	1.75	16.06
P-5	0.057	0.76	0.36	0.37	1.80	15.04
P-6	0.061	0.77	0.34	0.36	1.62	13.47
P-7	0.047	0.72	0.33	0.37	1.29	15.39
P-8	0.057	0.76	0.30	0.32	1.58	13.77
P-9	0.065	0.80	0.26	0.275	1.595	12.64
P-10	0.068	0.81	0.23	0.21	1.811	15.48
P-11	0.071	0.79	0.29	0.31	1.542	14.53
P-12	0.071	0.82	0.23	0.22	1.391	14.92

TABLE 6: Rotor flux prediction (LSTM with mu = 0.9).

Cluster	Response time (s)	Rho	Flux density		Error	
			Actual	Pden	RMSE	RF%
P-1	0.0093	0.17	0.32	0.33	1.29	13.27
P-2	0.0097	0.18	0.39	0.38	1.58	14.04
P-3	0.0098	0.18	0.39	0.40	1.811	13.81
P-4	0.0103	0.23	0.45	0.43	1.43	13.47
P-5	0.0122	0.26	0.47	0.46	1.56	13.75
P-6	0.0198	0.29	0.48	0.48	1.68	13.78
P-7	0.0213	0.33	0.51	0.52	1.63	20.81
P-8	0.0236	0.35	0.56	0.57	1.46	12.35
P-9	0.0292	0.38	0.58	0.59	1.51	13.17
P-10	0.0311	0.40	0.63	0.64	1.54	12.49
P-11	0.0414	0.46	0.71	0.69	1.56	16.65
P-12	0.0446	0.49	0.68	0.70	1.40	16.22

TABLE 7: Rotor flux prediction (LSTM with mu = 0.8).

Cluster	Response time (s)	Rho	Flux density		Error	
			Actual	Pden	RMSE	RF%
P-1	0.016	0.27	0.26	0.25	1.223	11.09
P-2	0.014	0.28	0.28	0.28	1.467	11.17
P-3	0.016	0.305	0.31	0.33	1.631	11.32
P-4	0.023	0.31	0.316	0.32	1.033	12.03
P-5	0.020	0.35	0.34	0.35	1.216	11.91
P-6	0.027	0.38	0.37	0.36	1.314	11.37
P-7	0.028	0.38	0.41	0.41	1.617	11.61
P-8	0.037	0.39	0.40	0.41	1.491	12.09
P-9	0.044	0.41	0.62	0.57	1.223	12.11
P-10	0.045	0.42	0.63	0.61	1.206	13.43
P-11	0.049	0.46	0.64	0.63	1.191	11.07
P-12	0.052	0.49	0.67	0.67	1.227	13.29

Table 8 shows the LSTM model evaluation with mu = 0.27. Five different models such as Vanilla LSTM, Bidirectional LSTM, CNN LSTM, and ConvLSTM are evaluated for training and testing of trajectory path in DTC. It is observed that ConvLSTM possesses lowest RMSE of 0.0018 and mean average error of 0.00112 with 150000 obs/s. The block diagram for long short-term memory (LSTM)-enabled direct torque control (DTC) for induction motor (IM) is shown in Figure 18. In this method, the actual torque and the stator flux are calculated in LSTM-enabled DTC control block using stator currents and voltages. These calculated torque and stator flux values are compared with the respective reference values to get the respective errors. Depending upon the values these errors, the triggering pulses for VSI are generated and fed to the VSI to generate the required voltage. The position of the voltage vector in state space can be determined in the same DTC block. Although ConvLSTM took large time for training, prediction accuracy is highest among all the LSTM algorithms. Residual

Table 8: LSTM model evaluation with mu = 0.27.

LSTM model	RMSE	R2- error	MSE	MAE	Prediction speed	Training time	Prediction accuracy
Vanilla	0.0093	1.0	$8.74e-5$	0.006417	150000 obs/s	17.312 s	83.82
Stacked	0.0037	1.0	$1.421e-5$	0.00277	250000 obs/s	29.58 s	89.05
Bidirectional	0.0064	1.0	$4.16e-5$	0.0046	160000 obs/s	31.239 s	86.99
CNN	0.0181	0.99	0.00032	0.0142	53000 obs/s	73.11 s	87.63
Conv	0.0018	1.0	$3.48e-5$	0.00112	150000 obs/s	91.16 s	91.81
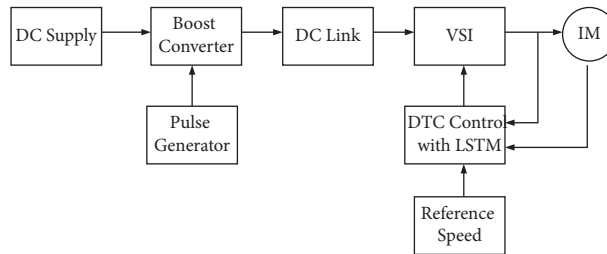
Figure 18: Block diagram for long short-term memory (LSTM)-enabled direct torque control (DTC) for induction motor.

(a)

(b)

(c)

(d)
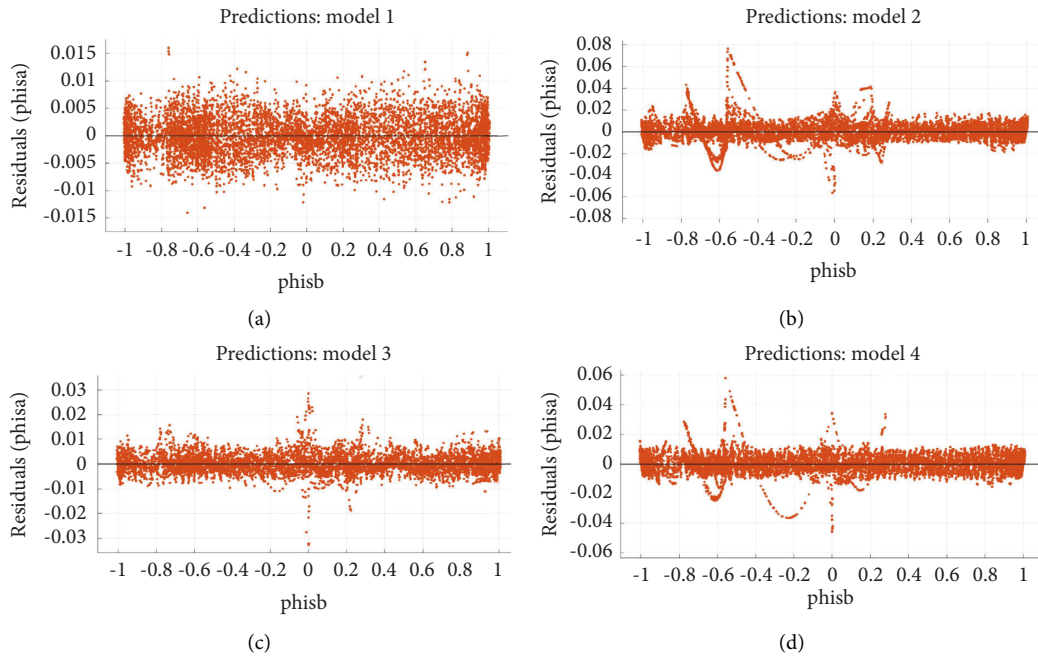
Figure 19: Training and testing of torque trajectory using LSTM: (a) model prediction with mu = 0.22; (b) model prediction with mu = 0.24; (c) model prediction with mu = 0.25; (d) model prediction with mu = 0.27.

validation for ConvLSTM is shown in Figure 19. Four different validation and residual models are presented for four different samples. In Figure 19(a), maximum deviation occurs between −0.005 and 0.005. Therefore, the prediction level is highly robust. Figures 19(b)–19(d) represent the validation and residual for samples 2, 3, and 4. Regression analysis for ConvLSTM is shown in Figure 20. Two different training models are analyzed for $R = 0.99471$ and $R = 0.99924$. Figure 20(b) shows that the training is close to the trajectory path, and hence the LSTM model is validated and is ready for loop in test. Figure 21 shows the histogram for regression analysis.

Figure 22(a) shows the gradient training operation for induction motor torque at an epoch of 519. The mean gradient variation ranged from 10^{-2} to 10^0. About 72,369-point-based sample training has been carried out to fit the training and testing data. Figure 22(b) shows the validation check for each test point with change in slope rate of −0.27. It is observed that not a single sample failed in testing for entire 519 epochs. Figure 22(c) shows the mean squared error performance curve for 519 epochs. The best training performance is 0.0142 at epoch 519.

Figure 23 shows the torque graph performance for LSTM-based DTC. Here it is found that a slight transient
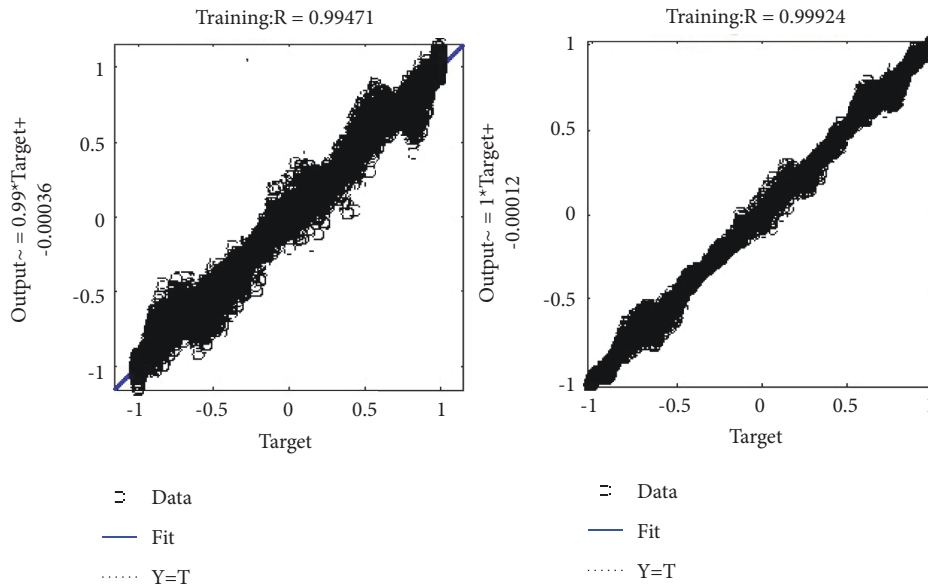
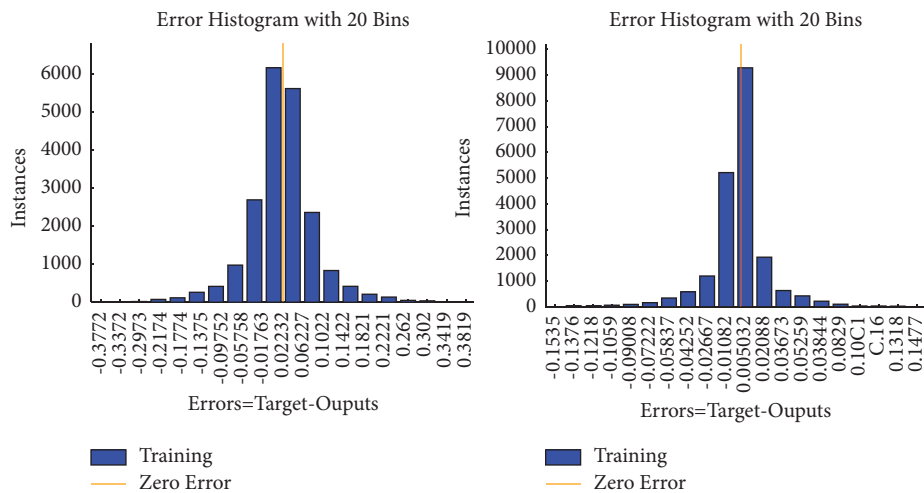Figure 20: Regression analysis for LSTM at (a) $R = 0.99471$ and (b) $R = 0.99924$.

Figure 21: Histogram for regression analysis.

performance change occurs at 16 N-m of torque. This is due to training of LSTM. At about 0.048 seconds, LSTM starts working towards tracking of trajectories. Figure 24 shows the performance of induction motor in terms of speed. Initially, an overshoot of 11.21% has been observed, and finally at 0.3 seconds, it settled down to the reference speed of 100 RPM. A small perturb has been noticed at 0.5 seconds to demonstrate the dynamic behaviour of controller. This analysis does not consider the dynamic change in stator resistance.

Figure 25 shows the induction motor stator flux performance under dynamic condition. The zoomed version of trajectory path clearly shows that a smooth stator flux has been achieved, thereby avoiding the vibration in the system during state change in torque.

Figure 26 represents the vibration measured at cage surface in induction motor due to interaction of stator flux and rotor flux. It is observed that due to interaction of two fluxes in the DTC technique, the vibration does not affect much as compared to fuzzy and ANFIS. This is because of 60-degree overlapping operation of stator voltage state.

As compared to fuzzy-DTC and ANFIS-DTC, the LSTM-enabled DTC shows better performance in terms of THD level. Like other controllers, here THD level has been measured at 21 Hz of fundamental frequency, which is measured to be 6.61% and is shown in Figure 27. This reduction in THD level is due to the pretrained load-dependent LSTM network which forecasts the flux density well in advance of the actual flux density. As a result, the switching pulses also work in proportion to the supplied current and load.

Table 8 shows a detailed comparative analysis of computation time for fuzzy-DTC, ANFIS-DTC, and LSTM-DTC. It is observed that LSTM-DTC takes 17% extra time as
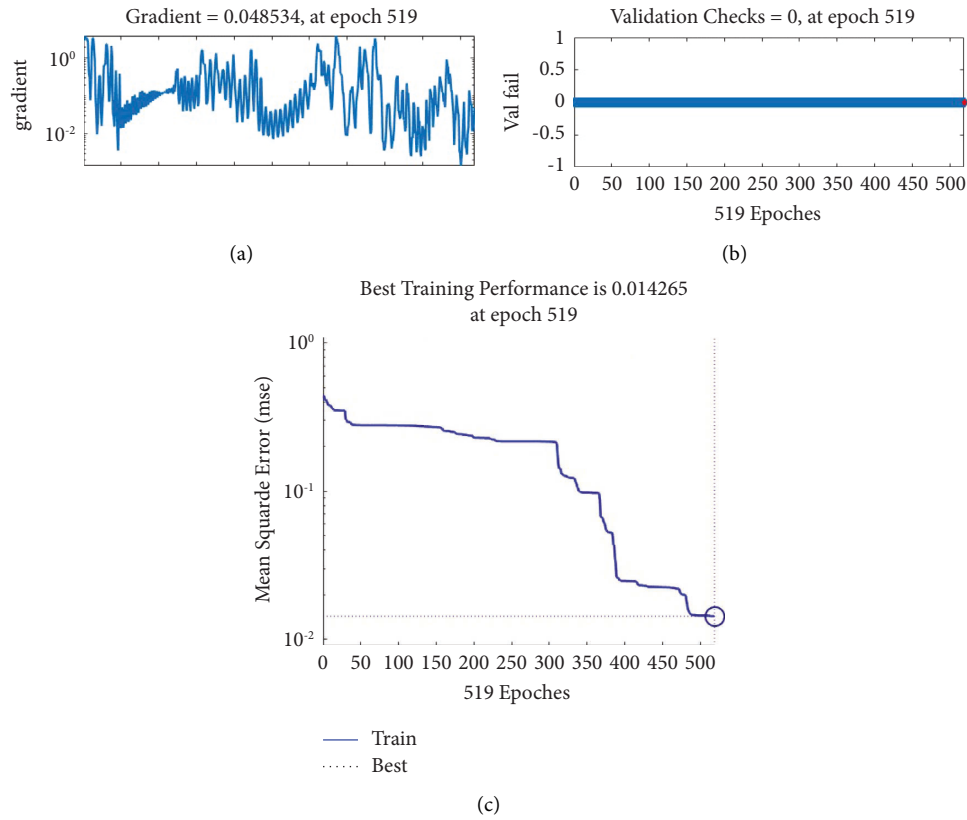
(a)

(b)

(c)

FIGURE 22: Training pattern analysis for LSTM: (a) gradient training; (b) validation check; (c) MSE performance.
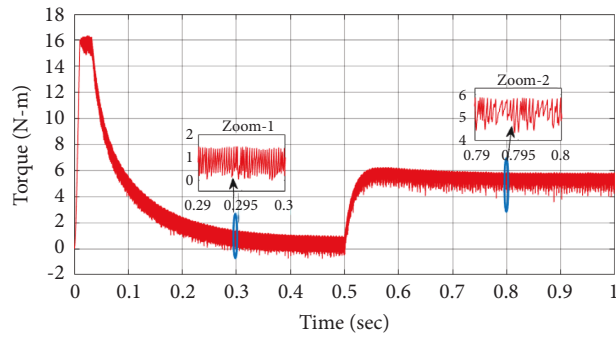

FIGURE 23: Induction motor torque performance based on LSTM-DTC.
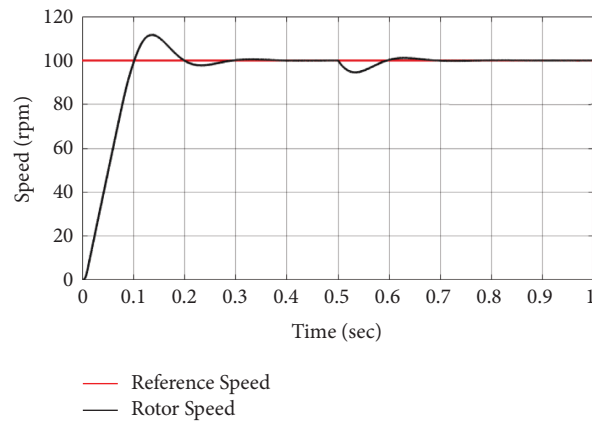

FIGURE 24: Induction motor speed performance based on LSTM-DTC.
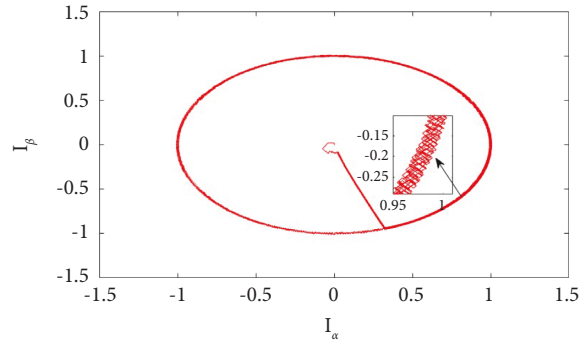
Figure 25: Induction motor stator flux performance based on LSTM-DTC.
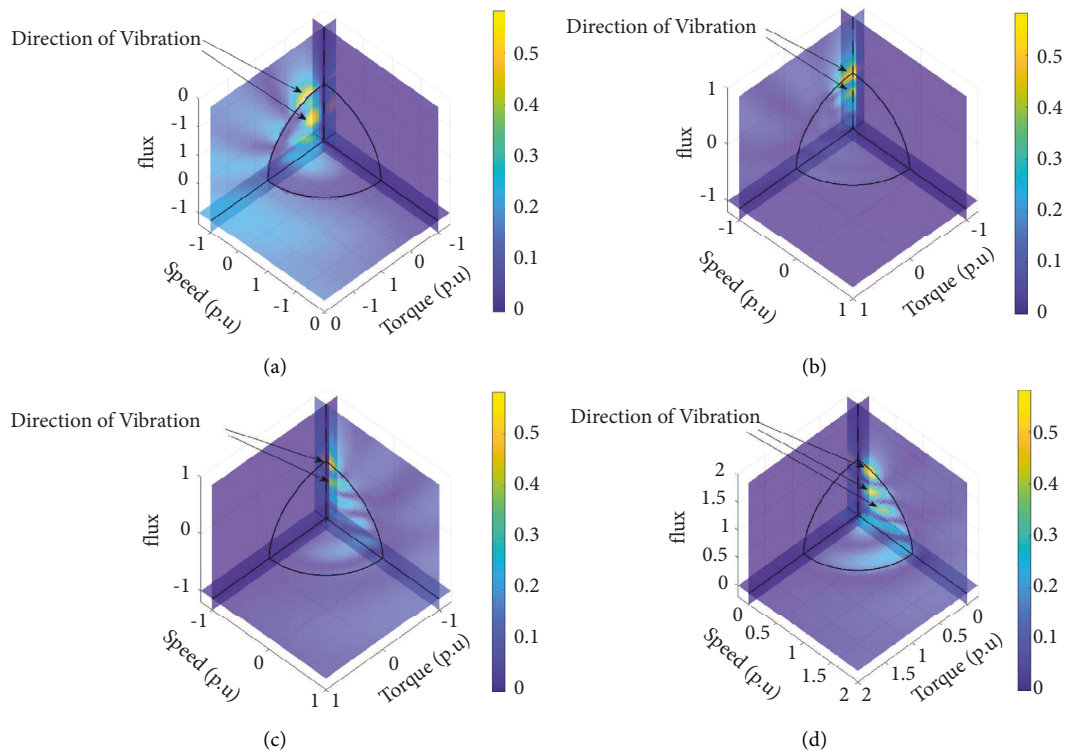

(a)

(b)

(c)

(d)

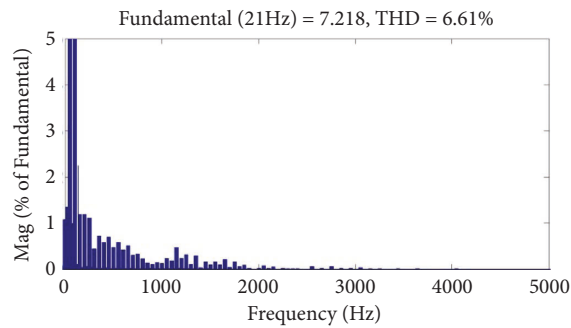Figure 26: Vibration measurement in IM cage due to interaction of stator flux and rotor flux.

Figure 27: THD of voltage under ConvLSTM-DTC.

TABLE 9: Comparative analysis of computation time for fuzzy-DTC, ANFIS-DTC, and LSTM-DTC.

Sr. no.	Name	Fuzzy-DTC	ANFIS-DTC	LSTM-DTC
1	Training general	276 ms	233 ms	241 ms
2	Prediction general	25 ms	19 ms	14 ms
3	Training specific	191 ms	117 ms	93 ms
4	Prediction specific	12 ms	11 ms	11 ms
5	Upper boundary detection	17 ms	14 ms	11 ms
6	Lower boundary detection	32 ms	31 ms	28 ms
7	Time to change PI parameter	93 ms	56 ms	47 ms
8	Stator flux control time	5.17 ms	3.94 ms	2.15 ms
9	Ave. time of training	218 ms	171 ms	126 ms
10	Ave. time of prediction	9.3 ms	7.8 ms	4.0 ms

compared to ANFIS-DTC during the training general condition, whereas the average time of prediction has drastically reduced from 9.3 ms in fuzzy-DTC to 4.0 ms in LSTM-DTC. Similarly, the time to change the PI controller parameter is also reduced to 47 ms.

5. Conclusion

In this paper, a novel ripple minimization technique has been presented for direct torque control of induction motor. As compared to fuzzy and ANFIS, the proposed ConvLSTM provides global minimal RMS torque ripple.

It is observed from Table 9 that LSTM-DTC has taken 2.15 ms to control stator flux against 5.17 ms and 3.94 ms as observed from fuzzy-DTC and ANFIS-DTC, respectively. The tuning parameters such as Proportional and Integral gain place an important role in the system with the use of LSTM enabled PI controller.The time has drastically reduced to 47 ms against 93 ms in fuzzy-DTC. Similarly the stator flux trajectory has helped the algorithm to propose the tinning parameter well in advance before the occurrence of actual situation, which is not there in fuzzy-DTC. The additional use of hysteresis controller is an added advantage to the LSTM controller to maintain the trajectory inside the boundary while predicting the tuning parameter for PI controller.

Parameter evaluation, reference frame transformation, and voltage sector selection can be easily achieved with LSTM. Here the sample rate required for direct torque control is typically in the range of 4–6 kHz. Continuously variable switching frequency can be achieved over a wide range of voltage distribution. Again, from Figure 19, it is observed that with mu = 0.27, the residuals are more scattered with respect to phisb. This clearly represents that all the data points for stator flux are independent from each other, which also leads to the totempole in achieving the uniform flux distribution. 60-degree voltage vector overlapping operation can be handled with the proposed method up to 3 operations in every 10 cycles. Excess overlapping may increase stress in the motor insulation.

The comparative model among the different LSTM models shows that the Stacked and Conv models are more close to each other; however, from prediction speed point of view, convolution techniques provide more accurate result among other techniques.

Data Availability

The data used to support the findings of this study are available from the corresponding author upon request.

Conflicts of Interest

The authors declare that they have no conflicts of interest.

References

[1] I. Takahashi and T. Noguchi, "Take a look back upon the past decade of direct torque control [of induction motors]," in *Proceedings of the IECON'97 23rd International Conference on Industrial Electronics, Control, and Instrumentation (Cat. No.97CH36066)*, vol. 2, pp. 546–551, New Orleans, LA, USA, November, 1997.

[2] Z. Wang, T. W. Ching, S. Huang, H. Wang, and T. Xu, "Challenges faced by electric vehicle motors and their solutions," *IEEE Access*, vol. 9, pp. 5228–5249, 2021.

[3] A. Anuchin, A. Bogdanov, G. Demidova, D. Savkin, K. Fedorova, and M. Gulyaeva, "Model predictive control of a direct current motor utilizing lookup tables," in *Proceedings of the 2020 XI International Conference on Electrical Power Drive Systems (ICEPDS)*, pp. 1–4, Saint Petersburg, Russia, October, 2020.

[4] N. El Ouanjli, A. Derouich, A. El Ghzizal et al., "Modern improvement techniques of direct torque control for induction motor drives-a review," *Protection and Control of Modern Power Systems*, vol. 4, no. 1, pp. 11-12, 2019.

[5] S. Mahfoud, A. Derouich, N. El Ouanjli, T. Mohammed, and A. Hanafi, "Field oriented control of doubly fed induction motor using speed sliding mode controller," in *E3S web of conferences*vol. 229, EDP Sciences, Article ID 01061, 2021.

[6] M. Elmahfoud, B. Bossoufi, M. Taoussi, N. El Ouanjli, and A. Derouich, "Rotor field oriented control of doubly fed induction motor," in *Proceedings of the 2019 5th International Conference on Optimization and Applications (ICOA)*, pp. 1–6, IEEE, Kenitra, Morocco, 2019, April.

[7] D. Ramasubramanian and V. Vittal, "Positive sequence induction motor speed control drive model for time-domain simulations," *IET Generation, Transmission & Distribution*, vol. 11, no. 7, pp. 1809–1819, 2017.

[8] A. Hmidet and O. Boubaker, "Real-time low-cost speed monitoring and control of three-phase induction motor via a voltage/frequency control approach," *Mathematical Problems in Engineering*, vol. 2020, Article ID 6913813, 14 pages, 2020.

[9] S. Abderazak and N. Farid, "Comparative study between Sliding mode controller and Fuzzy Sliding mode controller in

a speed control for doubly fed induction motor," in *Proceedings of the 2016 4th International Conference on Control Engineering Information Technology (CEIT)*, pp. 1–6, IEEE, Hammamet, Tunisia, 2016, December.

[10] N. El Ouanjli, A. Derouich, A. El Ghzizal, A. Chebabhi, and M. Taoussi, "A comparative study between FOC and DTC control of the doubly fed induction motor (DFIM)," in *Proceedings of the 2017 International Conference on Electrical and Information Technologies (ICEIT)*, pp. 1–6, IEEE, Rabat-Morocco, 2017, November.

[11] S. Zhang, S. Li, L. He, J. A. Restrepo, and T. G. Habetler, "Rotor Thermal Monitoring Scheme for Direct-Torque-Controlled Interior Permanent Magnet Synchronous Machines via High-Frequency Rotating Flux or Torque Injection," 2021, https://arxiv.org/abs/2106.02116.

[12] S. Zhang, S. Li, L. He, J. A. Restrepo, and T. G. Habetler, "A high-frequency torque injection-based rotor thermal monitoring scheme for direct-torque-controlled interior permanent magnet synchronous machines," in *Proceedings of the2017 IEEE Energy Conversion Congress and Exposition (ECCE)*, pp. 3552–3558, IEEE, Vancouver, British Columbia, Canada, 2017, October.

[13] S. Zhang, S. Li, L. He, J. A. Restrepo, and T. G. Habetler, "A high-frequency rotating flux injection based rotor thermal monitoring scheme for direct-torque-controlled interior permanent magnet synchronous machines," in *Proceedings of the 2017 IEEE International Electric Machines and Drives Conference (IEMDC)*, pp. 1–6, IEEE, Miami, Florida, USA, 2017, May.

[14] W. M. Hamanah, A. S. Salem, M. A. Abido, F. A. Al-Sulaiman, A. M. Qwbaiban, and T. G. Habetler, "Modeling, implementing, and evaluating of an advanced dual Axis heliostat drive system," *Journal of Solar Energy Engineering*, vol. 144, no. 4, Article ID 041001, 2022.

[15] R. R. Hete, S. K. Mishra, R. Dash, A. Ballaji, V. Subburaj, and K Jyotheeswara Reddy, "Analysis of DFIG-STATCOM P2P control action using simulated annealing techniques," *Heliyon*, vol. 8, no. 3, Article ID e09008, 2022.

[16] Z. Li, Y. Guo, J. Xia, H. Li, and X. Zhang, "Variable sampling frequency model predictive torque control for VSI-fed im drives without current sensors," *IEEE Journal of Emerging and Selected Topics in Power Electronics*, vol. 9, no. 2, pp. 1507–1517, 2021.

[17] C. Wu, Y. Jiao, H. Nian, and F. Blaabjerg, "A simplified stator frequency and power control method of DFIG-DC system without stator voltage and current sensors," *IEEE Transactions on Power Electronics*, vol. 35, no. 6, pp. 5562–5566, 2020.

[18] W. Wang, H. Yan, Y. Xu et al., "New three-phase current reconstruction for PMSM drive with hybrid space vector pulsewidth modulation technique," *IEEE Transactions on Power Electronics*, vol. 36, no. 1, pp. 662–673, 2021.

[19] S. Suresh and P. Rajeevan, "Virtual space vector-based direct torque control schemes for induction motor drives," *IEEE Transactions on Industry Applications*, vol. 56, no. 3, pp. 2719–2728, 2020.

[20] C. Patel, P. P. Rajeevan, A. Dey, R. Ramchand, K. Gopakumar, and M. P. Kazmierkowski, "Fast direct torque control of an open-end induction motor drive using 12-sided polygonal voltage space vectors," *IEEE Transactions on Power Electronics*, vol. 27, no. 1, pp. 400–410, 2012.

[21] S. G. Petkar and V. K. Thippiripati, "A novel duty controlled DTC of a surface PMSM drive with reduced torque and flux ripples," *IEEE Transactions on Industrial Electronics*, pp. 1–11, 2022.

[22] T. Zhu, X. Cao, Q. Yu, Z. Deng, and Z. Hao, "Direct torque control with phase commutation optimization for single-winding bearingless switched reluctance motor," *IEEE Transactions on Power Electronics*, vol. 37, no. 11, pp. 13238–13249, 2022.

[23] A. Dendouga, A. Guezi, and A. Bendaikha, "Robustness Evaluation of Fuzzy Logic Control Based on Feedback Linearization of Induction Motor Fed by Matrix Converter," in *Proceedings of the 2022 5th International Conference on Power Electronics and their Applications (ICPEA)*, pp. 1–7, Hail, Saudi Arabia, March, 2022.

[24] A. Yang and Z. Lu, "Multi-scalar model based predictive torque control without weighting factors and current sensors for induction motor drives," *IEEE Journal of Emerging and Selected Topics in Power Electronics*, vol. 10, no. 5, pp. 5785–5797, 2022.

[25] A. K. Kushwaha and A. K. Sharma, "Direct torque control based induction machines for speed-torque regulation," in *Proceedings of the 2022 8th International Conference on Advanced Computing and Communication Systems (ICACCS)*, pp. 778–781, Coimbatore, India, March, 2022.

[26] L. Huang, J. Ji, W. Zhao, T. Tao, and J. Cui, "Duty-ratio-based direct torque control with enhanced harmonic current suppression for dual-three-phase permanent magnet motor," *IEEE Transactions on Power Electronics*, vol. 37, no. 9, pp. 11098–11108, 2022.

[27] G.-M. Sung, C.-T. Lee, C.-C. Huang, and H.-Y. Hsieh, "Predictive direct torque control application-specific integrated circuit with a fuzzy proportional–integral–derivative controller and a new round-off algorithm," *IEEE Access*, vol. 10, pp. 48141–48152, 2022.

[28] U. R. Muduli, R. K. Behera, K. Al Hosani, and M. S. E. Moursi, "Direct torque control with constant switching frequency for three-to-five phase direct matrix converter fed five-phase induction motor drive," *IEEE Transactions on Power Electronics*, vol. 37, no. 9, pp. 11019–11033, 2022.

[29] H. Hadla and F. Santos, "Performance comparison of field-oriented control, direct torque control, and model-predictive control for SynRMs," *Chinese Journal of Electrical Engineering*, vol. 8, no. 1, pp. 24–37, 2022.

[30] R. Kennel, A. El-refaei, F. Elkady, S. Mahmoud, and E. Elkholy, "Torque ripple minimization for induction motor drives with direct torque control (DTC)," in *Proceedings of the Fifth International Conference on Power Electronics and Drive Systems, 2003. PEDS 2003*, pp. 210–215, Singapore, November, 2003.

[31] B. Mei, H. Liu, and J. Zhang, "Study of fuzzy control in direct torque control system," in *Proceedings of the 2009 International Conference on Artificial Intelligence and Computational Intelligence*, pp. 129–132, Shanghai, China, November, 2009.

[32] T. Geyer, G. Papafotiou, and M. Morari, "Model predictive direct torque control—Part I: concept algorithm and analysis," *IEEE Transactions on Industrial Electronics*, vol. 56, no. 6, pp. 1894–1905, 2009.

[33] G. Papafotiou, J. Kley, K. G. Papadopoulos, P. Bohren, and M. Morari, "Model predictive direct torque control—Part II: implementation and experimental evaluation," *IEEE Transactions on Industrial Electronics*, vol. 56, no. 6, pp. 1906–1915, 2009.

[34] N. S. Prakash and R. Ramchand, "Constant switching frequency DTC for induction motor fed from two level voltage source inverter," in *Proceedings of the 2014 IEEE International Conference on Power Electronics, Drives and Energy Systems (PEDES)*, pp. 1–5, Mumbai, India, December, 2014.

[35] X. Sun, T. Li, M. Yao, G. Lei, Y. Guo, and J. Zhu, "Improved finite-control-set model predictive control with virtual vectors for PMSHM drives," *IEEE Transactions on Energy Conversion*, vol. 37, no. 3, pp. 1–1894, 2021.

[36] X. Sun, T. Li, X. Tian, and J. Zhu, "Fault-tolerant operation of a six-phase permanent magnet synchronous hub motor based on model predictive current control with virtual voltage vectors," *IEEE Transactions on Energy Conversion*, vol. 37, no. 1, pp. 337–346, 2022.

[37] X. Sun, Y. Zhang, G. Lei, Y. Guo, and J. Zhu, "An improved deadbeat predictive stator flux control with reduced-order disturbance observer for in-wheel PMSMs," *IEEE/ASME Transactions on Mechatronics*, vol. 27, no. 2, pp. 690–700, 2022.

[38] X. Sun, T. Li, Z. Zhu, G. Lei, Y. Guo, and J. Zhu, "Speed sensorless model predictive current control based on finite position set for PMSHM drives," *IEEE Transactions on Transportation Electrification*, vol. 7, no. 4, pp. 2743–2752, 2021.

[39] S. Sahoo, S. Chandra Swain, and R. Dash, "A Novel Flower Pollination Method for Unit Price Estimation in a Microgrid," in *Proceedings of the 2022 3rd International Conference for Emerging Technology (INCET)*, pp. 1–5, Karnataka, India, May, 2022.

[40] A. Ballaji, R. Dash, V. Subburaj, J. R. Kalvakurthi, D. Swain, and S. C. Swain, "Design & development of MPPT using PSO with predefined search space based on fuzzy fokker planck solution," *IEEE Access*, vol. 10, pp. 80764–80783, 2022.